Surface & Coatings Technology 395 (2020) 125922

Contents lists available at ScienceDirect

Surface & Coatings Technology

journal homepage: www.elsevier.com/locate/surfcoat

Comparing physiologically relevant corrosion performances of Mg AZ31 alloy protected by ALD and sputter coated TiO_2

Mirco Peron*, Abdulla Bin Afif, Anup Dadlani, Filippo Berto, Jan Torgersen

Department of Mechanical and Industrial Engineering, Norwegian University of Science and Technology, Richard Birkelands vei 2b, 7034 Trondheim, Norway

ARTICLE INFO

Keywords:
Magnesium alloys
Temporary metallic implants
Corrosion resistance
Biocompatible coatings
Atomic Layer Deposition (ALD)
Sputter

ABSTRACT

The utilization of Mg alloys for biomedical applications is so far underexplored due to the accelerated corrosion hampering patient recovery post implantation. Here, we explore the effectiveness of corrosion reduction of an AZ31 alloy in Simulated Body Fluid when coated with a 40 nm sputtered TiO_2 layer and compare it to a similar coating made by Atomic Layer Deposition (ALD). Potentiodynamic polarization and hydrogen evolution experiments were performed on coated samples having different surface roughness and 3D topologies. Interestingly, ALD layers reduce corrosion current density by 94% on Ra = 118.6 ± 5.1 nm and 93% on Ra = 4794.3 ± 49.4 nm, whereas sputtered only by 84% on Ra = 118.6 ± 5.1 nm and 60% on Ra = 4794.3 ± 49.4 nm. Particularly on 3D aspects, the ALD coatings are superior, where a scaffold of 85% porosity with 1 mm pore sizes released 68% lower hydrogen compared to the sputtered counterparts. We relate these observations to the higher surface integrity, adhesion strength and lower line-of-sight restrictions of ALD compared to sputter deposition. The results can be interesting for researchers and practitioners aiming to make Mg alloys more commonplace as temporary metallic implant materials.

1. Introduction

The ageing of our society paired with increasing obesity raises the demand for orthopedic interventions requiring the implantation of medical devices [1]. Among these procedures, the number of orthopedic implantations is growing the fastest [2]. The materials currently used in orthopedic surgery are usually permanent metallic materials, such as stainless steel, titanium, and cobalt-chromium alloys [3] due to their high strength and good corrosion resistance [3–5]. However, two key issues arise with such materials. Firstly, the vast difference in elastic modulus compared to human bone results in the occurrence of stress-shielding phenomenon [6–12]. Secondly, to avoid possible long-term complications such as local inflammations [13–17], the implant shall ideally vanish when the healing process is completed. However common metallic implants are permanent and thus remain in the body. When complications arise, additional surgeries are required to remove the implant causing an increase in costs to the health care system, as well as emotional stress to the patient.

Biodegradable metallic materials may resolve these issues. Here, Mg and its alloys are promising candidates [18–21] due to their low density and an elastic modulus compatible with natural bone that minimize the risk of stress shielding [19]. In addition, Mg is abundant in the human body [22], essential for metabolism, is a cofactor for many enzymes [23] and supports the growth of tissues via the release of Mg^{2+} ions during its degradation. Despite their highly attractive properties, Mg and its alloys have not yet been used as implant materials because of their high corrosion rates in physiological environments, which may result in a loss of mechanical integrity and in hydrogen evolution beyond what bone tissue is able to accommodate. Yet, Mg's high corrosion rates in physiological environments yield a loss of mechanical integrity before healing is complete and triggers hydrogen evolution beyond what bone tissue can accommodate. Designed porosity and surface roughness sought to enhance osseointegration and cell adhesion on today's implants [24–26] further enhances corrosion and makes this material impractical for biomedical applications.

In the last several years, two main possibilities of reducing Mg's corrosion rate have been studied: 1) severe plastic deformation (SPD) and 2) coatings. Dealing with 1), either (a) the entire bulk or (b) the surface only can be subjected to SPD. Regarding (a), the corrosion current density can be reduced by almost two orders of magnitude [27–30] but it requires bulk property changes that might hamper the match to physiological conditions. Regarding (b), the authors reported a one order of magnitude current density reduction after cryogenic machining [31]. However, they also observed a rapid increase of corrosion upon removal of the surface layer.

A potential Mg implant may need surface texture and porosity to

* Corresponding author.
E-mail address: mirco.peron@ntnu.no (M. Peron).

https://doi.org/10.1016/j.surfcoat.2020.125922
Received 17 March 2020; Received in revised form 20 April 2020; Accepted 13 May 2020
Available online 15 May 2020

enhance ingrowth of cells and tissue at the patient specific site of interest [32,33]. In such a scenario, cryogenic machining, despite its benefits in initial corrosion resistance, might not be applicable as (1) intricate features are difficult to be made and (2) the resulting surfaces are smooth without texture. Hence an alternative, surface confined approach might be required that allows the control of surface texture. Coatings have thus emerged as an effective way to preserve designed macroscopic porosity and surface roughness tailored for osseointegration and to match mechanical characteristics [34,35]. Particularly sputtering has been studied due to the possibility to carry out the deposition at low temperatures, making the coating relatively insensitive to thermal expansion mismatches between the substrate and the coating, that are reported to affect the protectiveness of the coating due to the formation of cracks [36,37]. Jin et al. reported that the application of a 600 nm thick TaN layer on WE43 alloy reduced the corrosion current density in Simulated Body Fluid (SBF) by two orders of magnitude [38]. Ref. [39] reports a similar improvement when coating a WE43 alloy with 30 nm of TiN. However, the effectiveness of sputtering can be limited as it is subject to the line-of-sight. When considering implants, their complex shapes such as notches, pores and undercuts cannot be entirely coated due to this limitation, rendering corrosion most severe at places that are not accessible to the coating process.

Atomic Layer Deposition (ALD), in contrast, is not limited by the line-of-sight. Conformal, dense and pinhole-free films can be deposited on complex 3D substrates due to the self-limiting surface gas phase reactions; a technique newly explored for corrosion protection [40,41]. For example, Liu et al. reported a three orders of magnitude decrease in the corrosion current density of a 10 nm ZrO_2 coated AZ31 Mg alloy [40], while Yang et al. reported a two orders of magnitude corrosion current density reduction with a 40 nm ZrO_2 layer on a MgSr alloy [42].

Taking these results one step further, we explore the corrosion reduction of ALD layers on realistic AZ31 alloy implant surfaces and compare the results with those obtained by sputter technique. Specimens of different surface roughness (smooth and rough) and 3D topologies (flat and cube with pass-through holes) were coated with a 40 nm layer of TiO_2 by sputtering and ALD, respectively. The choice of the coating material felt on TiO_2 due to the high interest encountered in the biomedical field as a consequence of its high biocompatibility (it can induce in vitro bone-like apatite formation and stimulate osteoconductivity in vivo [43–45], along with the ability to bond directly and reliably to living bone in a short period after implantation [46]). The corrosion properties of the samples in SBF were evaluated by means of potentiodynamic polarization curves tests and hydrogen evolution experiments and were compared to bare samples for reference.

In addition, the chemical composition of the layer obtained by the two techniques was assessed by X-ray photoelectron spectroscopy (XPS) before and after 24 h of corrosion in SBF. The surface integrity of smooth and rough samples was assessed by a Scanning Electron Microscope (SEM).

2. Materials and methods

2.1. Sample preparation

AZ31 magnesium alloy was supplied in the form of commercially available bars (Dynamic Metals Ltd., Bedfordshire, UK). The microstructure was analyzed using a Leica DMRETM Optical Microscope (Leica microsystems, Wetzlar, Germany) after polishing the surface and etching it using a solution of alcohol (95 ml), picric acid (5 g), and acetic acid (10 ml). The microstructure is shown in Fig. 1 and consists of a homogeneous α matrix. The initial grain size was measured by linear intercept method which gave 14.8 ± 8 μm.

To simulate different biologically relevant conditions, flat discs (for potentiodynamic polarization curves) and plates (for hydrogen evolution experiments) with two different roughnesses and small cubes (for hydrogen evolution experiments) with pass-through holes to resemble the induced porosity in real implants have been machined. Discs with a diameter of 29 mm and a thickness of 2 mm (Fig. 2a) and 2 mm thick plates (60 mm long and 25 mm wide, Fig. 2b) were manufactured from the bars. The discs and the plates were then ground either using 40 grit silicon carbide papers to obtain a rough surface and up to 4000 grit silicon carbide papers to obtain a smooth surface. In the following, we will refer to the former group as “rough”, while to the latter as “smooth”. Both the typologies of samples were cleaned with acetone and ethanol for 5 min in an ultrasonic bath and then coated with a 40 nm TiO_2 layer using sputtering and ALD, respectively.

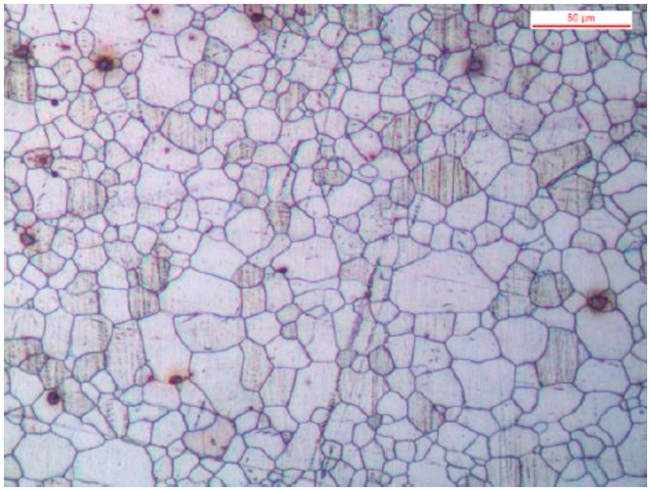

Fig. 1. Microstructure of the AZ31 alloy in the as-received condition.

The induced porosity of real implants has instead been resembled by manufacturing cubic samples of side 10 mm with six rows and six columns of equally spaced pass-through holes (φ = 1 mm) on each side (Fig. 2c) obtained by means of a CNC milling machine. After machining, the 3D samples were cleaned with acetone and ethanol for 5 min in an ultrasonic bath and then coated with a 40 nm TiO_2 layer using sputtering and ALD, respectively.

2.2. Sputtering

Thin film of TiO_2 is deposited using an AJA ATC-2200 V magnetron sputtering tool (AJA International Inc., MA, USA). The source used is 99.99% pure 2″ TiO_2 target. The sputtering chamber is pumped down to base pressure below 2e-7 Torr. Deposition is carried out with RF power of 63 W, at a pressure of 3mtorr with an Argon gas flow rate of 63 sccm. Initial depositions are conducted to determine the deposition rate, which is found to be 0.21 nm/min.

2.3. ALD

The ALD growth of TiO_2 thin film was conducted on a Savannah S200 system (Ultratech/Cambridge NanoTech, MA, USA), operating on thermal mode at reactor temperature of 160 °C. The metal organic precursor used was Tetrakis (dimethyl amido) titanium (IV) or TDMA-Ti, supplied by Sigma-Aldrich (Merck Life Sciences AS, Norway), heated at 75 °C and with deionized water as an oxidizer. Nitrogen was flown as a carrier gas at a constant flow rate of 20 sccm. The oxidant and precursor were pulsed in the following sequence, Water pulse 0.015 s, purge 5 s, TDMA-Ti precursor pulse 0.1 s and purge 5 s. SiO_2 witness wafers were also coated to determine the growth rate using a spectroscopic ellipsometry (Woollam M2000, J.A. Woollam, NE, USA). The growth rate was found to be 0.5 Å/cycle.

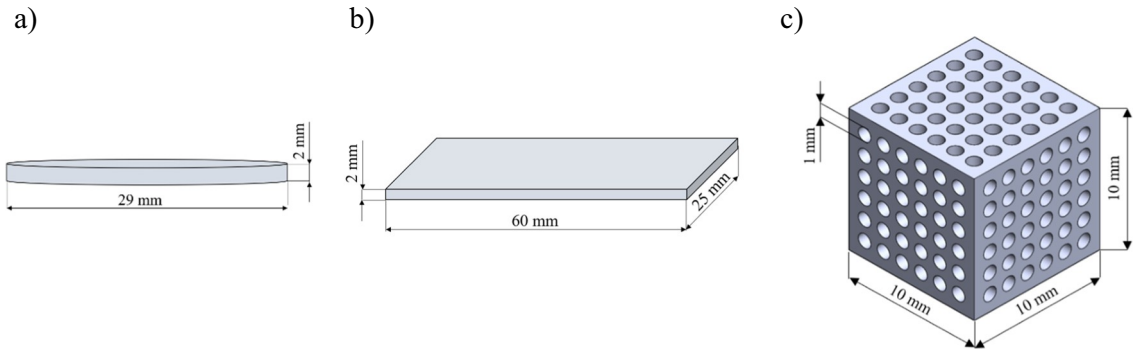

Fig. 2. Representation of the discs (a), plates (b) and 3D structures (c) used in the hydrogen evolution experiments.

2.4. Surface characterization

The roughness values of bare smooth and rough discs were measured using a Dektak 150 Profilometer (Veeco, AZ, USA). A linear scan was conducted in a hills and value mode. For calculating the Roughness average (R_a), an assessment length of 300 μm was defined, where an arithmetic average deviation from the mean line is calculated. Measurements were carried out on multiple points in the sample and an average value was calculated.

In addition, the surface integrity (amount and length of cracks) of sputtered and ALD smooth and rough coated discs was analyzed using FEI Quanta 450 Scanning electron Microscope (Thermo Fisher Scientific Inc., USA) with an acceleration voltage of 10 kV at a working distance of about 10 mm. Three samples for each condition, respectively, were assessed for reproducibility.

Finally, X-ray photoelectron spectroscopy (XPS) measurements were conducted to evaluate the chemical composition of the sputter and ALD coated samples. In addition, the chemical composition of the smooth samples coated by ALD and sputter, respectively, after 24 h of immersion in SBF was also assessed. Kratos Analytical XPS Microprobe (Kratos Analytical Ltd., Manchester, UK) which uses Al (Kα) radiation of 1486 eV in a vacuum environment of $5 * 10^{-9}$ Torr was used. CasaXPS software was used to analyze the XPS data.

2.5. Potentiodynamic polarization curves

Discs with a diameter of 29 mm and a thickness of 2 mm were manufactured as reported in Section 2.1. Potentiodynamic polarization tests were carried out on a Gamry Interface1000 potentiostat (Gamry Instruments, PA, USA) in order to compare the effectiveness of sputtered and ALD coatings in improving the corrosion resistance with different surface roughness. Bare samples were also tested as reference. The electrochemical tests used three-electrode equipment with the bare or coated samples as a working electrode, a Hg/Hg_2SO_4 electrode as a reference electrode, and a platinum plate electrode as a counter electrode. The samples were immersed in SBF solution (composition reported in Table 1). The temperature was set to 37 ± 1 °C to reproduce human body conditions. The potentiodynamic polarization curves were obtained applying a potential from ± 1 V with respect to the open circuit potential (OCP), obtained after a stabilization period of 30 min. The scan rate of the potentiodynamic polarization test was 0.5 mV/s. The area of the samples exposed to SBF was 1 cm^2 disregarding the surface roughness and the corrosion potential and corrosion current density was determined using the Tafel extrapolation method, according to the ASTM G5-14 standard [47]. The tests were repeated three times for each surface roughness.

2.6. Hydrogen evolution experiments

During the immersion tests, the chemical reaction between Mg and electrolyte occurs as shown in the following equation [19]:

$$Mg + 2H_2O \rightarrow Mg(OH)_2 + H_2 \quad (1)$$

From the above equation it can be easily understood that the dissolution of one magnesium atom generates one hydrogen gas molecule. In other words, the evolution of one mole of hydrogen gas corresponds to the dissolution of one mole of magnesium. Therefore, measuring the volume of hydrogen evolved allows to assess the corrosion rate of Mg and its alloys [49]. Hence, hydrogen evolution tests were used to compare the protection of sputter- and ALD- coated samples considering two different surface conditions each. To do so, the commercially available bars were manufactured into 2 mm thick plates (60 mm long and 25 mm wide) as described in Section 2.1. The samples were then immersed individually in 500 ml SBF at 37 °C for 72 h and the hydrogen bubbles were collected into a burette from each sample (Fig. 3), as suggested in Ref. [49]. The SBF was replaced with a fresh one every 24 h to limit the pH variations [50] that could have otherwise altered the corrosion behavior [51]. Bare “rough” and “smooth” samples were also tested as references, respectively.

In addition, hydrogen evolution tests were carried out on the cubic samples described in Section 2.1. These samples were used to compare the performances of sputter and ALD in the case of 3D structures that resemble the induced porosity in real implants. Bare samples were also tested as reference.

Table 1
Reagents and their quantities for preparation of 1000 ml of the SBF solution according to [48].

Reagents	Amount
NaCl	8.035 g
$NaHCO_3$	0.355 g
KCl	0.225 g
$K_2HPO_4{\cdot}3H_2O$	0.231 g
$MgCl_2{\cdot}6H_2O$	0.311 g
1.0_M-HCl	39 ml
$CaCl_2$	0.292 g
Na_2SO_4	0.072 g
Tris	6.118 g

2.7. Degradation behaviour

Bare and coated cylindrical and cubic samples, prepared as described in Sections 2.5 and 2.1, respectively, were soaked for one day in SBF at 37 °C to carry out macro- and micro-morphological characterizations before and after corrosion. All samples were ultrasonically cleaned for 5 min in acetone and ethanol, dried in the air, and then observed by means of Canon EOS 4000D (Canon, Tokyo, Japan) and FEI Quanta 450 Scanning Electron Microscope (Thermo Fisher Scientific Inc., USA) for macro- and micro-morphological characterizations, respectively. In addition, 3D samples after corrosion have been sliced to

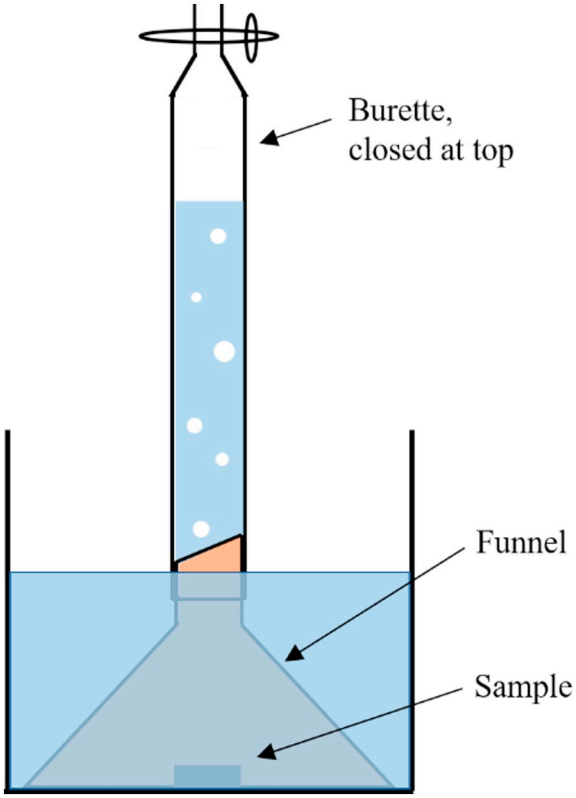

Fig. 3. Schematic illustration of the set-up for measurement of the volume of hydrogen evolved.

show the corroded aspect of the undercuts for bare, sputter coated and ALD coated samples.

3. Results

3.1. Surface characterization

3.1.1. Surface integrity

The presence of cracks on ALD and sputter smooth and rough discs has been assessed by means of SEM analyses and the representative images have been reported in Fig. 4. In addition, the average length and numerosity are reported in Table 2.

It can be noted that the number of cracks (crack density in Table 2) and the length of the cracks increased moving from smooth to rough samples. In addition, under the same conditions, sputter coated samples are shown to be characterized by more and longer cracks.

3.1.2. Roughness evaluation

The average surface roughness of the smooth bare samples was 118.6 ± 5.1 nm, while that of the rough bare samples was 4794.3 ± 49.4 nm.

3.1.3. XPS

3.1.3.1. Composition of the coating. XPS was conducted to determine the chemical composition of the ALD and sputter deposited TiO_2. The measurements were carried out on thin films deposited on Si wafer. To start with, etching was conducted on the surface to remove the effect of environmental contamination and surface oxidation. Surface was etched for 180 s with an ion beam energy of 2 KeV. Regional scans for the elements, titanium, O and C were carried out at high resolution. Negligible amounts of C were observed in the regional scan, thus indicating an ideal deposition without any process contamination. Fig. 5a and c are regional scans of titanium deposited using ALD and Sputter deposition techniques, respectively. The peaks are found to be very similar in both the deposition techniques. Peaks corresponding to the core level binding energies, 459 eV and 464 eV of Ti $2p_{3/2}$ and Ti $2p_{1/2}$ are observed, which is due to Ti^{4+} oxidation state in TiO_2 [52]. The shoulder at lower energy around 456 eV is due to the presence of Ti^{3+} caused by the argon etching step [53]. Fig. 5b and d are regional scans of the oxygen peak in ALD coated and sputter coated samples, respectively. The peak at 531 eV is due to oxygen atoms in TiO_2 phase [54], while the small shoulder at higher energy is due to O in –OH groups present in the form of impurities. Stoichiometric TiO_2 thin films should have Ti and oxygen in 1:2 ratio i.e. 66.7% O and 33.3% Ti, but in our case, we have found the composition to be around 60% for O and 40% Ti indicating an O deficient deposition in both cases (Table 3).

3.1.3.2. XPS after corrosion. The chemical composition of sputter and ALD coated smooth discs after 24 h of corrosion in SBF (Fig. 6) was evaluated using XPS and reported in Table 4. In this case, the main focus was on the number of chemical elements, and thus the binding energies were not assessed. Etching was conducted on the surface to remove the effect of environmental contamination and surface oxidation. The surface was etched for 180 s with an ion beam energy of 2 KeV. Regional scans for Mg, Ti and O were carried out at high resolution. In addition, Ca and P have also been assessed since Mg and its alloys are reported to form Mg (Ca) phosphates [55].

3.2. Potentiodynamic polarization tests

The potentiodynamic polarization curves of the AZ31 cylindrical rough and smooth samples plotted on a semi-logarithmic scale are shown in Figs. 7 and 8, respectively. Bare, sputter coated and ALD coated curves are reported in black, blue and red lines, respectively. The related kinetic and thermodynamic corrosion electrochemical characteristics are reported in Tables 5 and 6.

Considering both rough and smooth samples, the presence of TiO_2 coatings led to an improvement in corrosion resistance, namely an ennoblement of corrosion potential E_{corr} and a reduction of corrosion current density i_{corr} of more than one order of magnitude. It is worth noting that the corrosion current density is directly related to the corrosion rate by the Faraday's law, which expresses the material loss of the implant during its permanence into the human body. This implies that the application of coatings leads to a reduced corrosion rate. ALD coatings are shown to be more effective in the protection from corrosion, especially when a high surface roughness is considered.

3.3. Hydrogen evolution tests

The hydrogen evolution of rough and smooth plates is reported in Figs. 9 and 10, respectively. Bare, sputter coated and ALD coated hydrogen evolution are reported in black, blue and red lines, respectively.

The results of the hydrogen evolution tests are in line with the potentiodynamic polarization curves, i.e. the application of the coating decelerates the corrosion process, irrespective of the considered surface roughness. In addition, the difference in the efficiency of the sputter and ALD coatings is more visible in the rough samples, again in agreement with the potentiodynamic polarization curves.

The better performances of ALD compared to sputtering in reducing corrosion is further confirmed by the hydrogen evolution tests carried out on 3D structures reported in Fig. 11.

3.4. Degradation behavior

3.4.1. Cylindrical samples

Figs. 12 and 13 display the macro-morphologies of sputter and ALD coated cylindrical samples before and after one day of corrosion in SBF for smooth and rough samples, respectively. The bare AZ31 smooth and rough samples were taken as control.

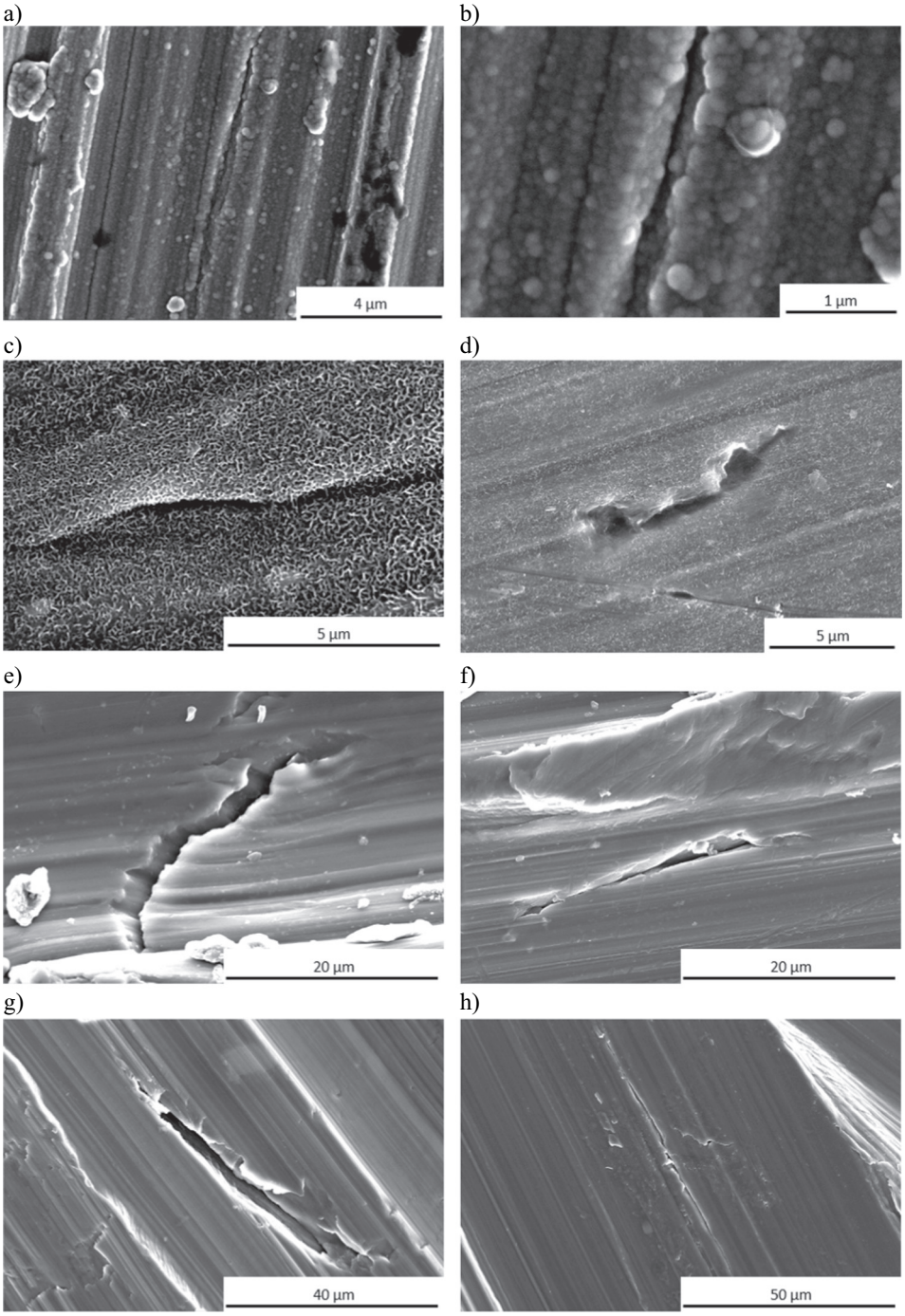

Fig. 4. SEM images of representative cracks formed on smooth ALD (a and b), smooth sputter (c and d), rough ALD (e and f) and rough sputter (g and h) discs. Since the size of cracks are different for each condition, the scale bars differ from picture to picture.

Table 2
Average crack length and density (meant as number of cracks per square centimetre) of the cracks detected for the different conditions.

	Smooth ALD	Smooth sputter	Rough ALD	Rough sputter
Crack length (µm)	4.54 ± 3.05	8.04 ± 2.48	23.59 ± 3.96	58.12 ± 7.25
Density (n° cracks/cm^2)	0.87 ± 0.37	1.71 ± 0.68	3.18 ± 0.62	5.3 ± 0.78

From the macro-morphologies it can be clearly seen that the degree of corrosion damage decreased with the application of coatings for both smooth and rough samples. In particular, the protectiveness of the ALD coating is shown to be higher since most of the TiO_2 coating is still present both in the smooth and rough samples, whereas several spots exposing the Mg substrate are visible on the sputter coated samples, particularly regarding the rough specimen. The higher protectiveness of the ALD coating are further confirmed by the micro-morphologies after corrosion of smooth and rough cylindrical samples, gathered in Figs. 14 and 15, respectively.

Table 3
Chemical composition of ALD and Sputter deposited TiO_2.

Deposition mode	O 1s	Ti 2p
ALD	60%	40%
Sputtering	61%	39%

In the micro-morphologies of ALD coated samples, wider un-corroded areas are visible compared to sputter coated and especially bare samples. This is even more evident when smooth samples are considered. For all the samples, the corroded areas have numerous cracks dividing the surface into a network structure, where the delamination

Table 4
Chemical composition of ALD and sputter smooth discs before and after 24 h of immersion in SBF.

Element	Concentration (%) before corrosion		Concentration (%) after corrosion	
	ALD	Sputter	ALD	Sputter
Mg	9	11	9	8
Ti	21	22	3	11
O	69	66	73	69
Ca	1	1	6	7
P	0	0	9	5

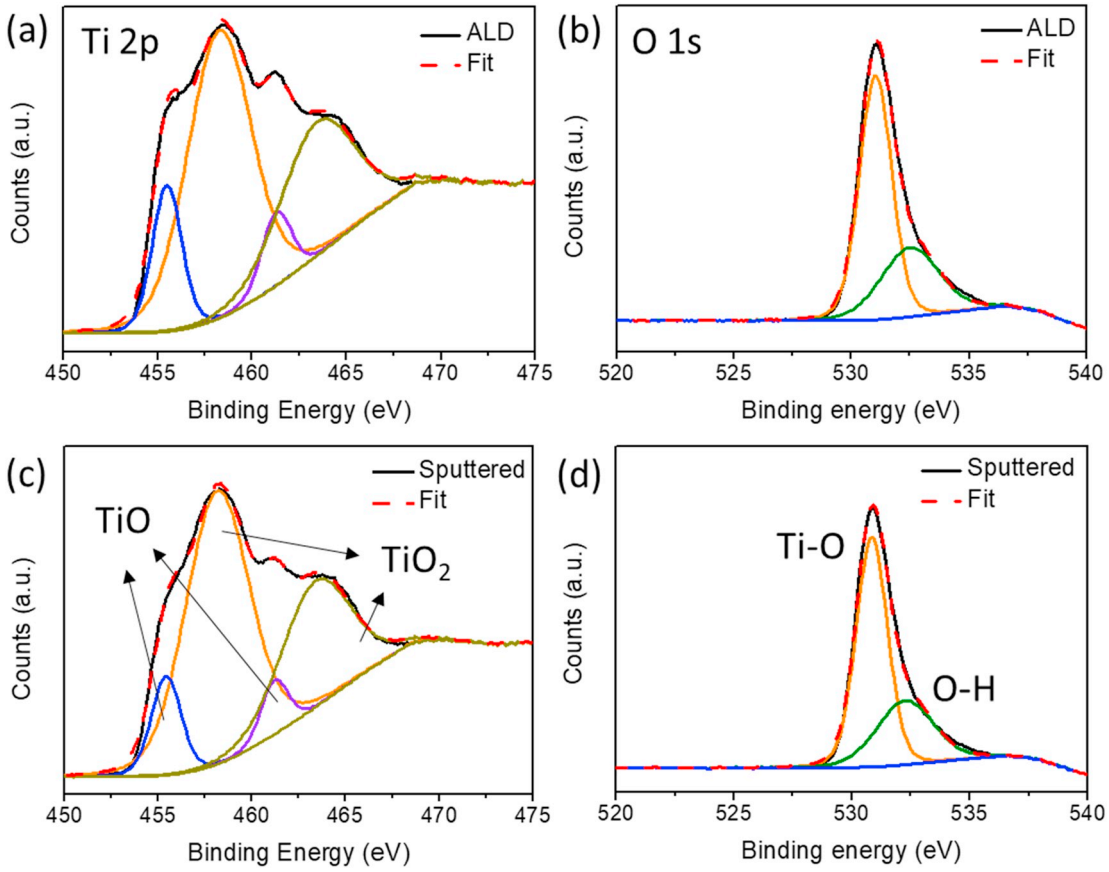

Fig. 5. XPS spectra for ALD deposited TiO_2 (a) Ti 2p (b) O 1s and Sputter deposited TiO_2 (c) Ti 2p (d) O 1s.

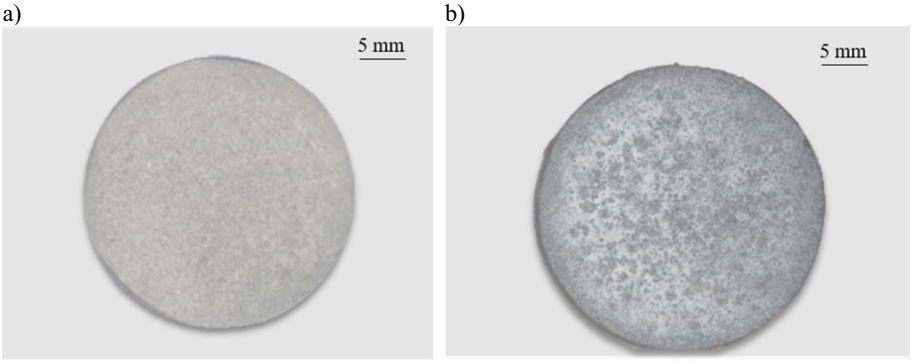

Fig. 6. Images of ALD (a) and sputter (b) coated smooth samples after 24 h of immersion in SBF.

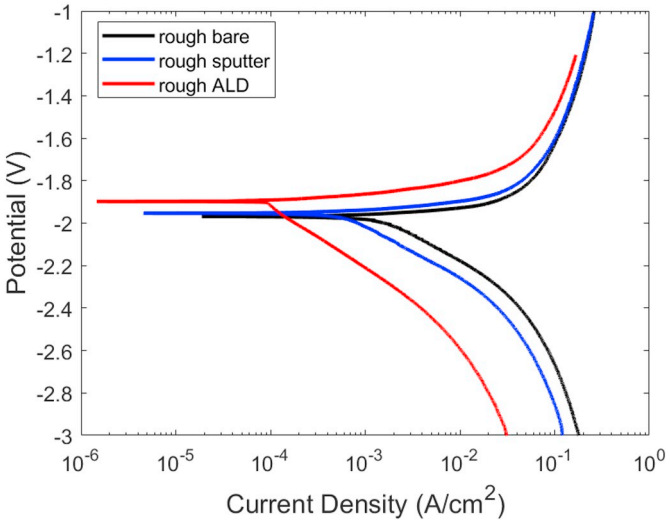

Fig. 7. Potentiodynamic polarization curves of rough samples.

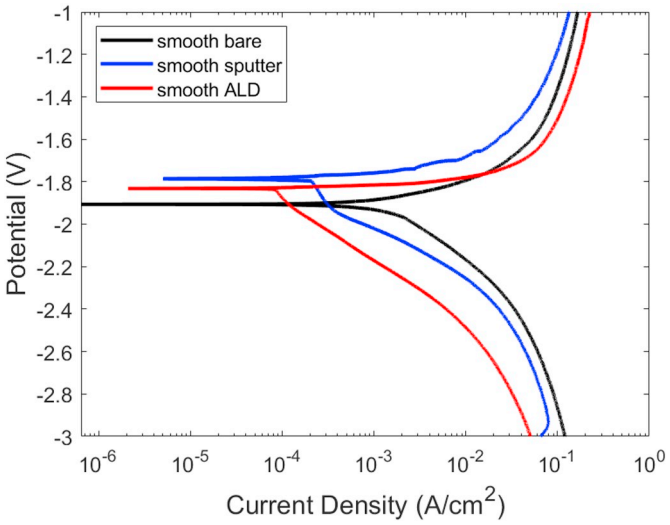

Fig. 8. Potentiodynamic polarization curves of smooth samples.

Table 5
Electrochemical corrosion data extrapolated from Fig. 7.

	Ecorr (V)	icorr (μA/cm^2)
Bare	−1.97 ± 0.025	1500 ± 40
Sputter coated	−1.95 ± 0.035	600 ± 10
ALD coated	−1.90 ± 0.015	102 ± 4

Table 6
Electrochemical corrosion data extrapolated from Fig. 8.

	Ecorr (V)	icorr (μA/cm^2)
Bare	−1.91 ± 0.02	1400 ± 25
Sputter coated	−1.79 ± 0.033	220 ± 15
ALD coated	−1.83 ± 0.016	84 ± 6

and the flaking off of the protective film can be observed.

3.4.2. 3D samples

The macro-morphologies of 3D bare, sputter coated and ALD coated samples before and after one day of corrosion in SBF are reported in Fig. 16.

The bare samples are highly corroded, rendering it difficult to

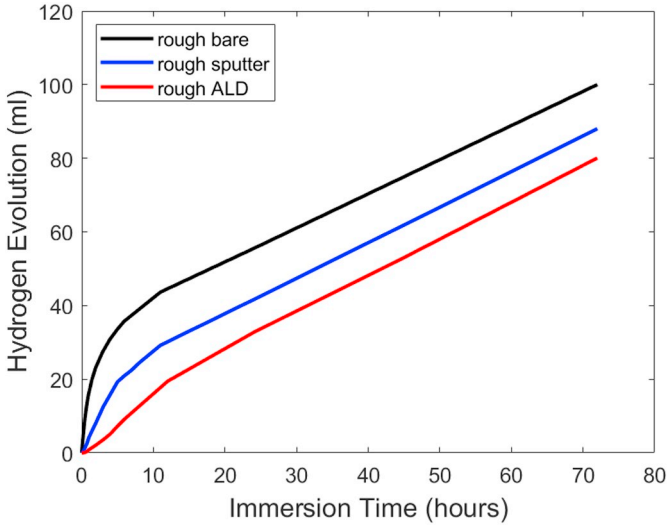

Fig. 9. Hydrogen evolution of rough samples.

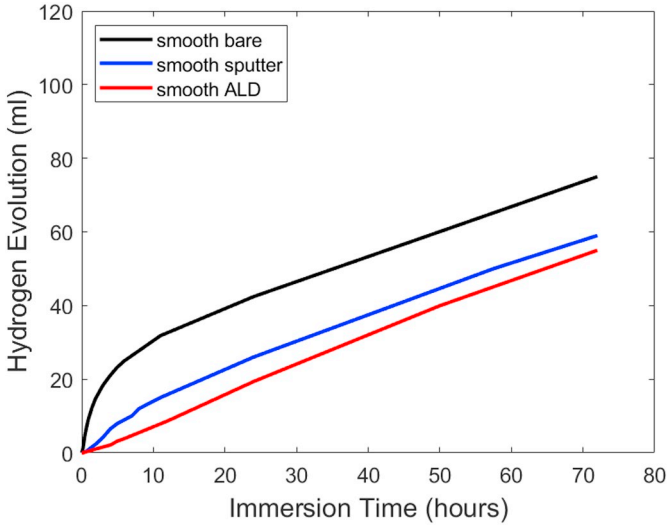

Fig. 10. Hydrogen evolution of smooth samples.

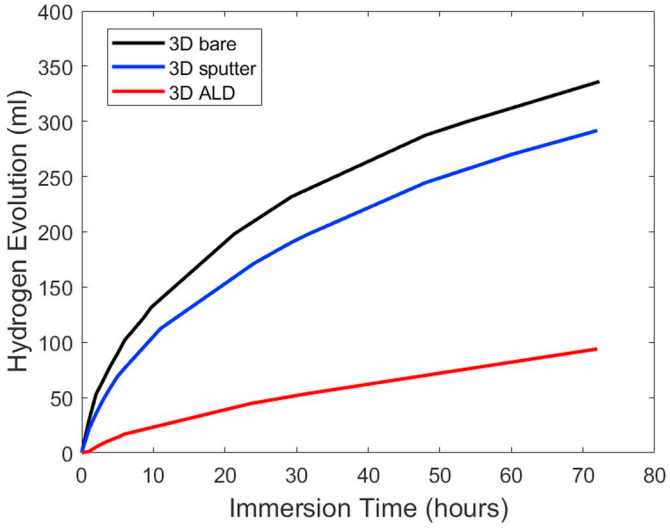

Fig. 11. Hydrogen evolution of the 3D structures reported in Fig. 2.

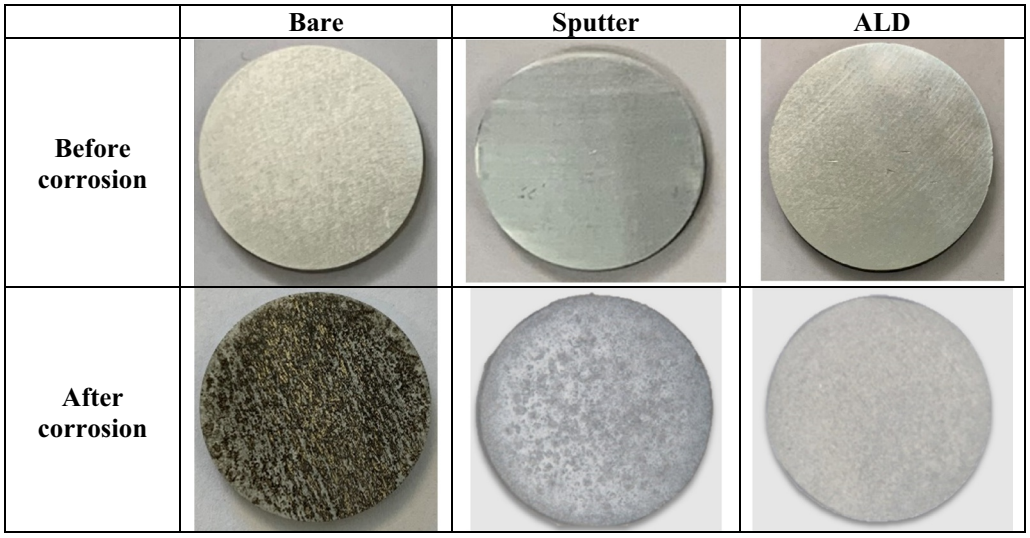

Fig. 12. Macro-morphologies of smooth bare, sputter and ALD TiO_2 coated samples before and after corrosion.

recognize the original shape. A reduction in corrosion is obtained by the application of coatings, particularly in the case of ALD coated samples. This is confirmed by the micro-morphologies of the corroded samples (Fig. 17). In fact, while for bare samples the structure is fully covered by corrosion products (Fig. 17a) and the original structure can be barely detected in some locations (in particular within the holes that are obstructed by the corrosion products (Fig. 17b)), the sputter coated samples are characterized by a lower amount of corrosion products (Fig. 17c) and the original structure can still be recognized retaining visible un-corroded areas (Fig. 17d). An even lower corrosion is detected in the ALD coated samples (Fig. 17e and f).

However, the improvement in corrosion resistance of sputter coated samples with respect to bare samples is not obvious when looking at the micro-morphology of the corroded sample's sliced cross-section (Fig. 18). The micro-morphologies of the corroded sputter 3D samples (Fig. 18b) are comparable to those of the bare counterparts (Fig. 18a). In ALD samples (Fig. 18c), in contrast, the corrosion seems consistently lower, which we attribute to the nature of the coating process providing effective barriers also within a given 3D aspect, independent from its topological and surface complexity.

4. Discussions

Macroscopic porosity and surface roughness are known to assist the surface attachment and growth of various cell types on implant surfaces [56,57]. A realistic biodegradable implant surface must possess these characteristics and must maintain its integrity during its designed lifetime. In an attempt to mimic such a scenario, we compared the corrosion reduction induced by TiO_2 sputtered and ALD layers on AZ31 implant surfaces with different surface roughness and induced macroscopic porosities through potentiodynamic polarization curves and hydrogen evolution tests.

Although both sputter and ALD TiO_2 40 nm coatings improve the corrosion resistance, their performances differ. Deviations increase with surface and topological complexity (roughness and porosity). Whereas the corrosion current density (i_{corr}) of ALD coated smooth samples differs by a factor of three compared to sputter coated counterparts, the i_{corr} is six times lower on ALD coated rough samples. These results are corroborated by hydrogen evolution experiments. After 72 h of exposure to SBF, the amount of evolved hydrogen from smooth samples coated with ALD is 6.8% lower than on sputter coated samples, while the difference is as high as 10% on rough samples.

The lower corrosion reduction of sputtered coatings on rough

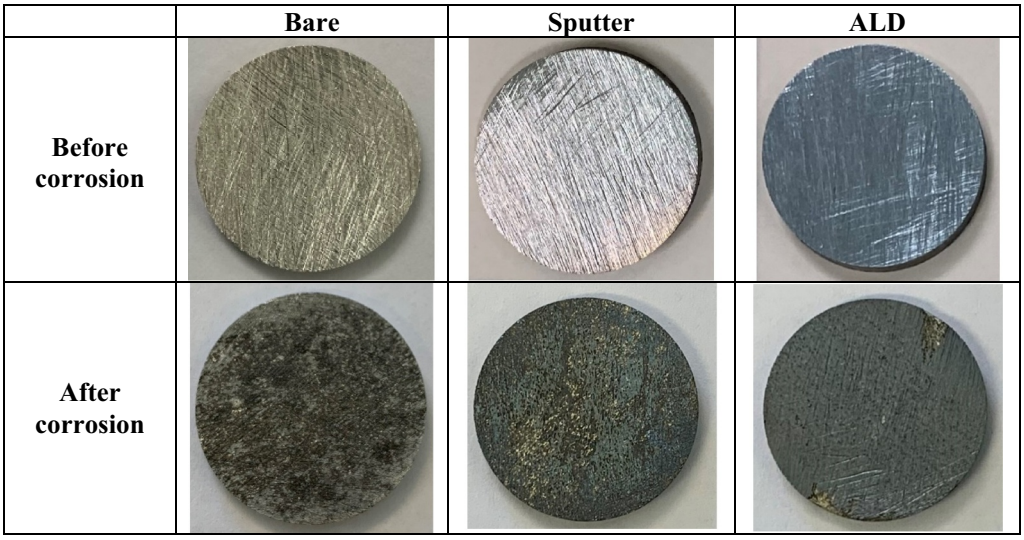

Fig. 13. Macro-morphologies of rough bare, sputter and ALD TiO_2 coated samples before and after corrosion.

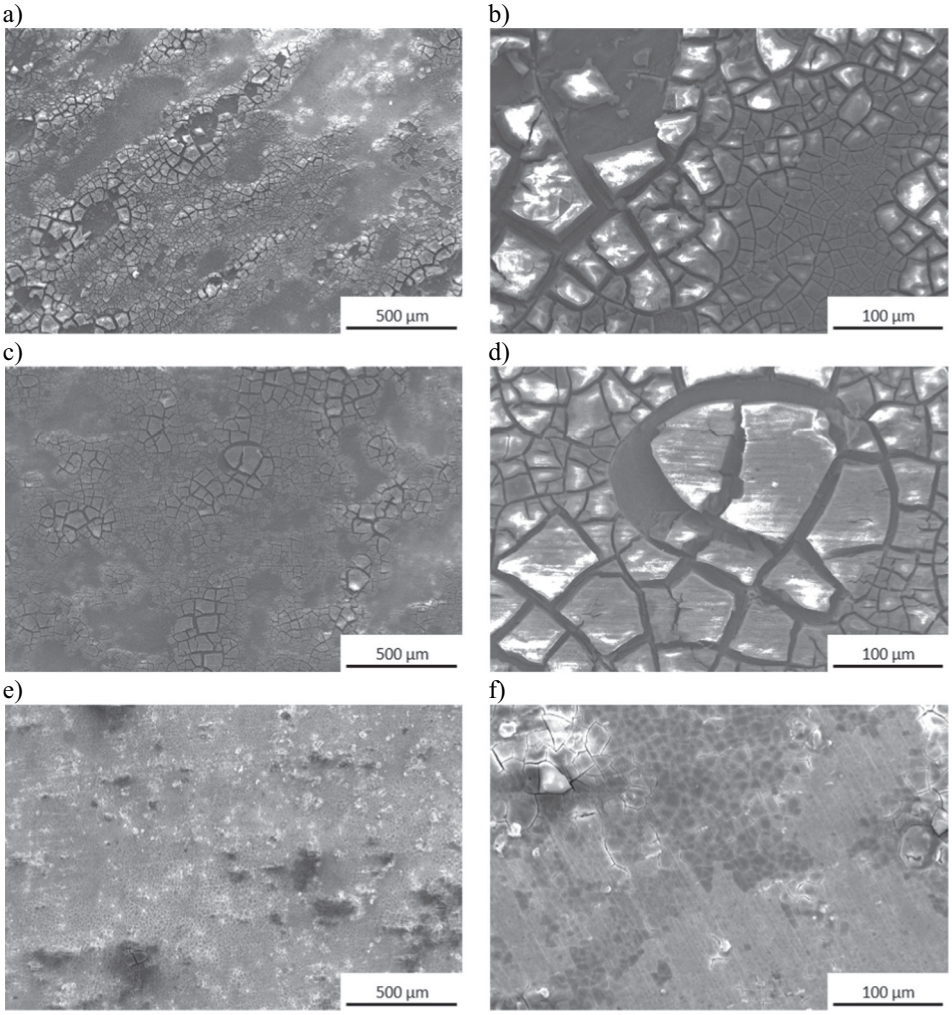

Fig. 14. Micro-morphologies of bare (a and b), sputter (c and d) and ALD (e and f) coated cylindrical smooth samples after corrosion.

surfaces is in agreement with the results of Munemasa and Kumakiri [58]. They reported that the corrosion protection of sputter coated carbon steel decreases with the increase in substrate roughness. They related this effect to an increased amount of uncovered surface area in the case of rougher substrates. Sputter is subject to line-of-sight limitations hindering complete surface coverage of areas shadowed by surface features. This becomes particularly problematic on 3D aspects in cell scaffolds that naturally provide 3D features as topological cues for cells to anchor and proliferate [59,60]. Our simple 3D porous structures possess several macroscopic undercuts and shadowed areas, which are likely superior for cell attachment as compared to flat surfaces. Here, the hydrogen evolution experiments show that the ALD coatings perform significantly better; the respective specimens are characterized by a 68% reduced hydrogen evolution compared to sputter coated counterparts. Interestingly, the SEM micrograph of the undercuts and shadowed areas of the sliced 3D structures reveals the sputter coated samples (Fig. 18b) to possess a similar morphology to bare samples (Fig. 18a). This indicates that these areas have not or only barely been covered in the first place. ALD coatings, instead, are conformal, and thus cover the inner areas of the structure (Fig. 18c). We hypothesize that this is the main contribution to the significant observed differences in degradation upon the internal structure's exposure to SBF.

The corrosion reduction with ALD compared to sputter coatings cannot be ascribed to the line-of-sight limitation only, but also to defects in the coating. Defects such as cracks and pores provide access for the media to attack the underlying substrate thereby reducing the coatings' effectiveness. If the coatings deposited were perfectly conformal, dense and defect-free, their corrosion rate would ideally match the literature reported values for pure TiO_2 in SBF. However, the corrosion rate of the sputter and ALD coated samples (measured by the Faraday's law [61] after normalization by the surface area) differs significantly from that of pure TiO_2 ($0.37{\cdot}10^{-6}$ mm/year) [62]. Smooth samples (characterized by a Sdr[1] of 0.06) have corrosion rates $1.8{\cdot}10^{-3}$ and $6.8{\cdot}10^{-4}$ mm/year for sputter and ALD coated samples, respectively, while rough samples (characterized by a Sdr of 0.1) have rates of $4.7{\cdot}10^{-3}$ and $8.1{\cdot}10^{-4}$ mm/year, respectively. The higher difference reported between the corrosion rate of sputter coated AZ31 samples and that of pure TiO_2 compared to that for ALD coated samples indicates a higher amount and size of defects in the sputtered TiO_2 coatings. This is corroborated by the surface integrity assessments of Fig. 4 and Table 2. The higher number of cracks shown for rough samples further increases the deviation in corrosion rate from pure and defect-free TiO_2.

Cracks usually form due to induced residual stresses in the coating resulting from thermal expansion coefficient differences between coating and substrate [63,64]. The thermal expansion coefficient of Mg is reported to be $27{\cdot}10^{-6}$ °C^{-1} [64], while that of TiO_2 is $7{\cdot}10^{-6}$ °C^{-1} [65,66]. The higher amount of cracks in the sputter coating may be attributed to the higher process temperature during sputtering (260 °C)

[1] Area roughness parameter, describes the additional area provided by texture with respect to the planar area [72].

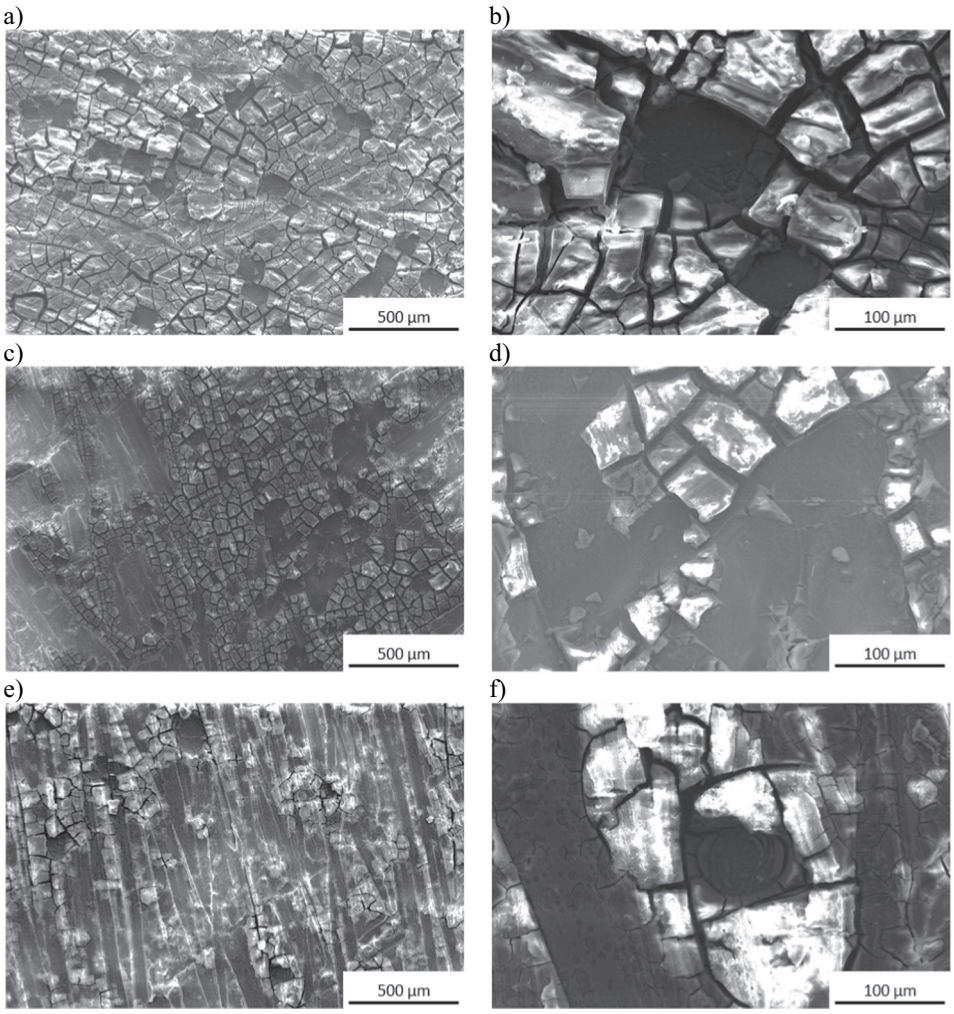

Fig. 15. Micro-morphologies of bare (a and b), sputter (c and d) and ALD (e and f) coated cylindrical rough samples after corrosion.

compared to ALD (160 °C) [67]. It is reported that higher residual stresses are to be expected with higher substrate roughness during the coating process [68,69]. This is reported to lead to a higher number and longer cracks [70], an observation that can be made in our rough samples too (Fig. 4 and Table 2).

The exposure of the Mg substrate on the flat samples can likely not be attributed to the cracks through the coating only. After 24 h of immersion in SBF sputter coated samples are characterized by large areas

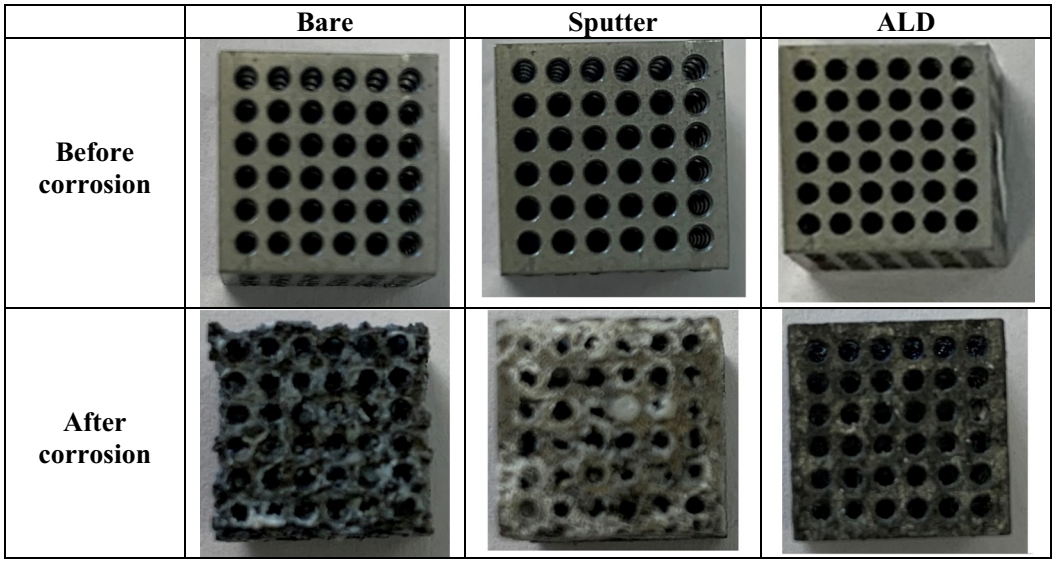

Fig. 16. Macro-morphologies of smooth bare, sputter and ALD TiO_2 coated samples before and after corrosion.

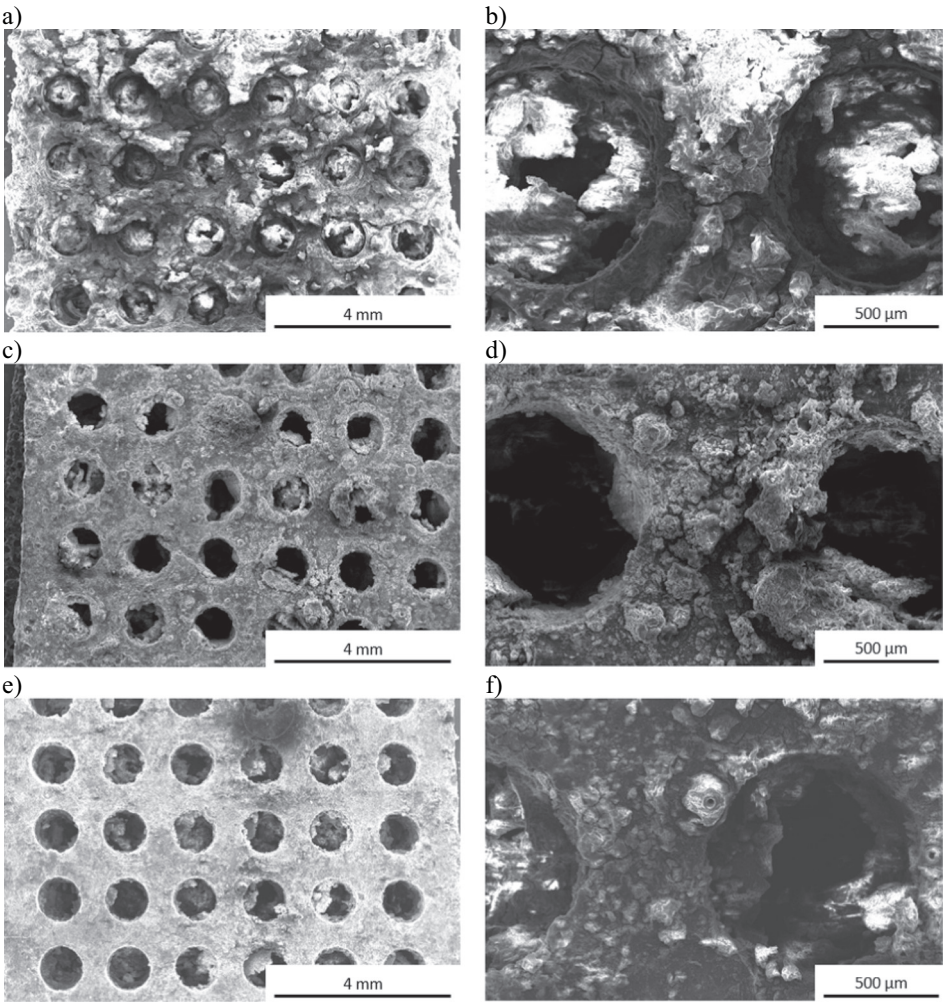

Fig. 17. Micro-morphologies of bare (a and b), sputter (c and d) and ALD (e and f) coated 3D samples after corrosion.

of the substrate obviously exposed to the corrosive environment (darker dots in Fig. 6b), which are not visible in ALD coated samples (Fig. 6a). These areas are of diameter (0.97 mm, StdDev 0.25 mm), which is significantly larger than the reduction of thickness in the bare samples after immersion in SBF for 24 h (thickness 0.12 mm StdDev 0.03 mm). We therefore hypothesize in-plane corrosion between substrate and coating has likely taken place facilitated by interfacial delamination as also reported elsewhere [71]. The ALD samples are instead characterized by a more uniform corrosion mode, indicative of a stronger film adhesion, as suggested also by the XPS measurements after corrosion. These measurements indicate that ALD films have a lower concentration of titanium after corrosion (3%, as compared to 21% before corrosion) and an unchanged amount of Mg. After 24 h of immersion, the Mg substrate coated by ALD has barely been affected with the corrosive media mainly attacking the TiO_2 layer. Contrarily, in the sputter coated samples, the corrosion is less uniform. A higher amount of Ti prevails after corrosion whereas Mg is reduced after immersion indicative of an attack on the underlying substrate.

We conclude that both coatings can be considered viable for the fabrication of biodegradable implants with a prolonged durability inside the human body. However, the choice of the coating technique has to be taken based on the specific scenario. Surface integrity of the coatings and an effective barrier in undercuts and shadowed areas render ALD superior in our study, which may have an impact on the choice of coating techniques for Mg based biomedical implants in the future.

5. Conclusions

In this work, we provided new insights into the corrosion performances of ALD coated AZ31 Mg alloy and compared corrosion protection performances of ALD and sputtered biocompatible TiO_2 coatings. As for a real implant, complex 3D geometry and surface texture are likely important for cell adhesion and ingrowth, we evaluated the corrosion protection performances on substrates with two different surface roughnesses as well as complex 3D architectures (designed porosity). All samples were coated with a 40 nm layer of TiO_2 by either sputter deposition or ALD and their corrosion properties have been evaluated by means of potentiodynamic polarization curves tests and hydrogen evolution experiments. The evaluation of the surface integrity (number and size of cracks) prior to the corrosion and the assessment of the chemical composition before and after corrosion are reported.

The main findings can be summarized as follows:

- The ALD technique provides better corrosion protection both for smooth and rough surfaces. Dealing with the former, the corrosion current density of bare samples has been reduced from 1400 µA/cm^2 to 220 µA/cm^2 and 84 µA/cm^2 using sputtering and ALD, respectively, while for rough samples, the corrosion current density of the bare material was reduced from 1500 µA/cm^2 to 600 µA/cm^2 and 102 µA/cm^2 using sputtering and ALD, respectively.
- A similar trend was obtained in hydrogen evolution tests. The hydrogen evolved from bare smooth samples was reduced by 21% and 27% with sputter and ALD, respectively. Dealing with rough

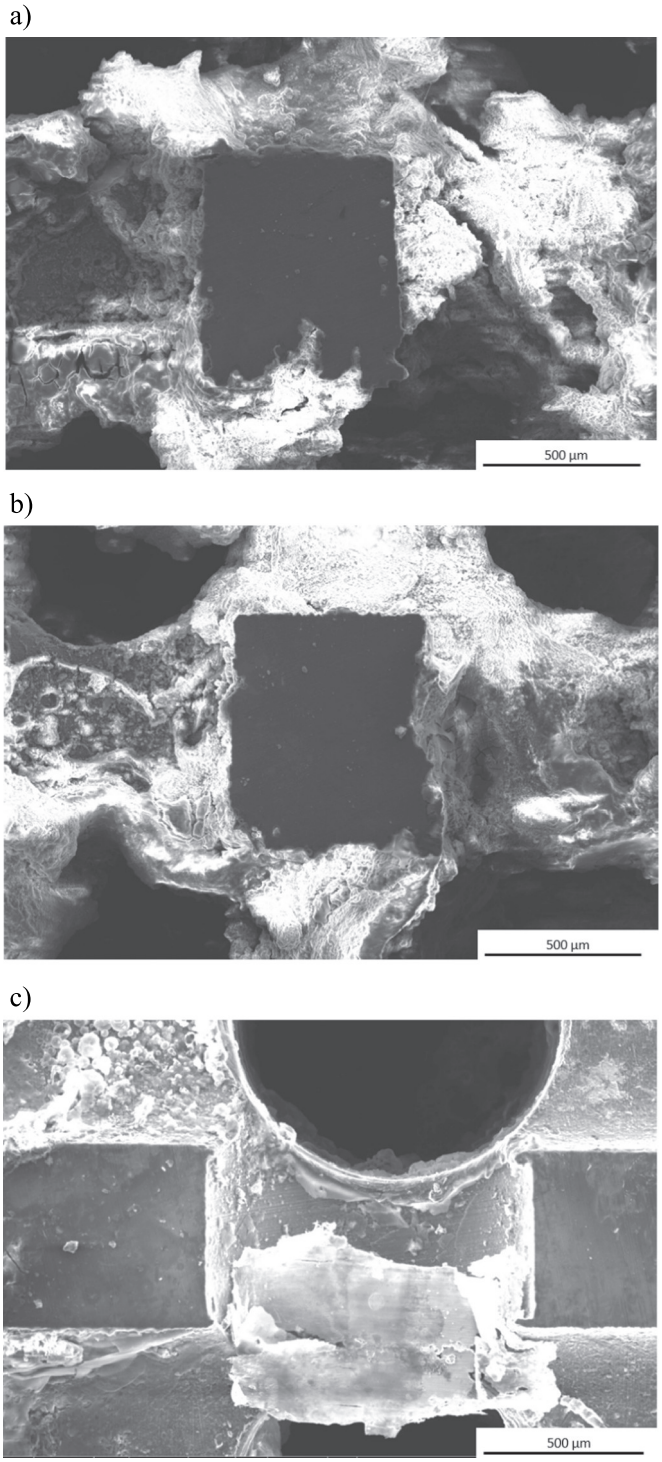

Fig. 18. Micro-morphology of the bare (a), sputter coated (b) and ALD coated (c) corroded sample's sliced cross-section.

samples, the hydrogen evolved from the bare material was reduced by 12% and 20% with sputter and ALD, respectively.

- The line-of-sight limitation of sputtering is particularly evident in the case of 3D porous structures, where the hydrogen evolved from the bare samples is reduced by 13% only with sputtering, while ALD coatings lead to a reduction of 72%.
- In the as-deposited condition, sputter coatings have more and longer cracks. Before corrosion, the composition of the sputter and ALD TiO_2 coating were identical, whereas after 24 h of corrosion, the amount of Ti and Mg differed. XPS results indicate a significantly higher decrease in the Ti concentration for the ALD coated samples after corrosion, whereas the Mg concentration remains unchanged. Instead, the sputter coating experiences a decrease in both Ti and Mg content indicating a corrosion attack on the underlying substrate as well as the remaining of parts of the protective TiO_2 layer on the substrate. We hence hypothesize that the improved corrosion performances of ALD cannot be attributed to the line-of-sight limitation only, but also to the coatings' surface integrity differences by either technology.

It can be concluded that both sputtering and ALD are effective coating techniques to increase the corrosion resistance of AZ31 alloy, but ALD has been shown to provide the lowest corrosion rates regardless of the surface conditions (roughness and topology). Therefore, the ALD technique can be considered viable for the fabrication of next-generation biodegradable implants with a prolonged durability inside the human body.

CRediT authorship contribution statement

Mirco Peron:Conceptualization, Data curation, Investigation, Methodology, Validation, Visualization, Writing - original draft, Writing - review & editing.**Abdulla Bin Afif**:Data curation, Investigation, Validation.**Anup Dadlani**:Data curation, Investigation, Validation.**Filippo Berto**:Supervision.**Jan Torgersen**:Supervision, Writing - original draft, Writing - review & editing.

Declaration of competing interest

The authors declare that they have no known competing financial interests or personal relationships that could have appeared to influence the work reported in this paper.

Acknowledgement

Abdulla Bin Afif was supported by NTNU's Enabling technologies: Nanotechnology. The Research Council of Norway is acknowledged for the support to the Norwegian Micro- and Nano-Fabrication Facility, NorFab, project number 245963/F50. Anup Dadlani was funded by the Norwegian Research Council under project number 274459 Translate.

References

[1] M.P. Ginebra, T. Traykova, J.A. Planell, Calcium phosphate cements as bone drug delivery systems: a review, J. Control. Release 113 (2006) 102–110, https://doi.org/10.1016/j.jconrel.2006.04.007.
[2] http://share.iofbonehealth.org/EU-6-Material/Reports/IOF%20Report_EU.pdf (web archive link, 20 November 2019), (n.d.). http://share.iofbonehealth.org/EU-6-Material/Reports/IOF Report_EU.pdf (accessed November 20, 2019).
[3] T. Hanawa, Overview of metals and applications, Met. Biomed. Devices, Elsevier, 2010, pp. 3–24, , https://doi.org/10.1533/9781845699246.1.3.
[4] T. Albrektsson, P.-I. Brånemark, H.-A. Hansson, J. Lindström, Osseointegrated titanium implants: *requirements for ensuring a long-lasting, direct bone-to-implant anchorage in man*, Acta Orthop. Scand. 52 (1981) 155–170, https://doi.org/10.3109/17453678108991776.
[5] F. Rossi, N.P. Lang, E. De Santis, F. Morelli, G. Favero, D. Botticelli, Bone-healing pattern at the surface of titanium implants: an experimental study in the dog, Clin. Oral Implants Res. 25 (2014) 124–131, https://doi.org/10.1111/clr.12097.
[6] T.W. Bauer, J. Schils, The pathology of total joint arthroplasty. II. Mechanisms of implant failure, Skelet. Radiol. 28 (1999) 483–497 http://www.ncbi.nlm.nih.gov/pubmed/10525792 , Accessed date: 31 March 2017.
[7] A.R. Dujovne, J.D. Bobyn, J.J. Krygier, J.E. Miller, C.E. Brooks, Mechanical compatibility of noncemented hip prostheses with the human femur, J. Arthroplast. 8 (1993) 7–22, https://doi.org/10.1016/S0883-5403(06)80102-6.
[8] C.A. Engh, J.D. Bobyn, The influence of stem size and extent of porous coating on femoral bone resorption after primary cementless hip arthroplasty, Clin. Orthop. Relat. Res. (1988) 7–28 http://www.ncbi.nlm.nih.gov/pubmed/3370887 , Accessed date: 31 March 2017.
[9] J. Kerner, R. Huiskes, G.H. van Lenthe, H. Weinans, B. van Rietbergen, C.A. Engh, A.A. Amis, Correlation between pre-operative periprosthetic bone density and post-operative bone loss in THA can be explained by strain-adaptive remodelling, J.

Biomech. 32 (1999) 695–703, https://doi.org/10.1016/S0021-9290(99)00041-X.
[10] D.R. Sumner, J.O. Galante, Determinants of stress shielding: design versus materials versus interface, Clin. Orthop. Relat. Res. (1992) 202–212 http://www.ncbi.nlm.nih.gov/pubmed/1729005 , Accessed date: 31 March 2017.
[11] T.M. Turner, D.R. Sumner, R.M. Urban, R. Igloria, J.O. Galante, Maintenance of proximal cortical bone with use of a less stiff femoral component in hemi-arthroplasty of the hip without cement. An investigation in a canine model at six months and two years, J. Bone Joint Surg. Am. 79 (1997) 1381–1390 http://www.ncbi.nlm.nih.gov/pubmed/9314401 , Accessed date: 31 March 2017.
[12] B. Van Rietbergen, R. Huiskes, H. Weinans, D.R. Sumner, T.M. Turner, J.O. Galante, The mechanism of bone remodeling and resorption around press-fitted THA stems, J. Biomech. 26 (1993) 369–382, https://doi.org/10.1016/0021-9290(93)90001-U.
[13] B.G. Pound, Corrosion behavior of metallic materials in biomedical applications. I. Ti and its alloys, 32 (2014) 1–20, https://doi.org/10.1515/corrrev-2014-0007.
[14] B.G. Pound, Corrosion behavior of metallic materials in biomedical applications. II. Stainless steels and Co-Cr alloys, 32 (2014) 21–41, https://doi.org/10.1515/corrrev-2014-0008.
[15] J.J. Jacobs, J.L. Gilbert, R.M. Urban, Corrosion of metal orthopaedic implants, J. Bone Joint Surg. Am. 80 (1998) 268–282 http://www.ncbi.nlm.nih.gov/pubmed/9486734 , Accessed date: 31 March 2017.
[16] J.J. Jacobs, N.J. Hallab, A.K. Skipor, R.M. Urban, Metal degradation products: a cause for concern in metal-metal bearings? Clin. Orthop. Relat. Res. (2003) 139–147, https://doi.org/10.1097/01.blo.0000096810.78689.62.
[17] I.B. Beech, J.A. Sunner, C.R. Arciola, P. Cristiani, Microbially-influenced corrosion: damage to prostheses, delight for bacteria, Int. J. Artif. Organs. 29 (2006) 443–452 http://www.ncbi.nlm.nih.gov/pubmed/16705614 , Accessed date: 20 June 2017.
[18] M. Peron, F. Berto, J. Torgersen, Magnesium and its Alloys as Implant Materials: Corrosion, Mechanical and Biological Performances, CRC Press LLC, 2020.
[19] M. Peron, J. Torgersen, F. Berto, Mg and its alloys for biomedical applications: exploring corrosion and its interplay with mechanical failure, Metals (Basel) 7 (2017) 252, https://doi.org/10.3390/met7070252.
[20] N. Li, Y. Zheng, Novel magnesium alloys developed for biomedical application: a review, J. Mater. Sci. Technol. 29 (2013) 489–502, https://doi.org/10.1016/J.JMST.2013.02.005.
[21] R.K. Singh Raman, S. Jafari, S.E. Harandi, Corrosion fatigue fracture of magnesium alloys in bioimplant applications: a review, Eng. Fract. Mech. 137 (2015) 97–108, https://doi.org/10.1016/j.engfracmech.2014.08.009.
[22] M.P. Staiger, A.M. Pietak, J. Huadmai, G. Dias, Magnesium and its alloys as orthopedic biomaterials: a review, Biomaterials 27 (2006) 1728–1734, https://doi.org/10.1016/j.biomaterials.2005.10.003.
[23] A.C. Hänzi, A.S. Sologubenko, P.J. Uggowitzer, Design strategy for new biodegradable Mg–Y–Zn alloys for medical applications, Int. J. Mater. Res. 100 (2009) 1127–1136, https://doi.org/10.3139/146.110157.
[24] M. Fraldi, L. Esposito, G. Perrella, A. Cutolo, S.C. Cowin, L. Esposito, Topological optimization in hip prosthesis design, Biomech. Model. Mechanobiol. 9 (2010) 389–402, https://doi.org/10.1007/s10237-009-0183-0.
[25] L.E. Murr, S.M. Gaytan, E. Martinez, F.R. Medina, R.B. Wicker, Fabricating functional Ti-alloy biomedical implants by additive manufacturing using electron beam melting, J. Biotechnol. Biomater. (2012) 2, https://doi.org/10.4172/2155-952X.1000131.
[26] A.-F. Obaton, J. Fain, M. Djemaï, D. Meinel, F. Léonard, E. Mahé, B. Lécuelle, J.-J. Fouchet, G. Bruno, In vivo XCT bone characterization of lattice structured implants fabricated by additive manufacturing, Heliyon 3 (2017), https://doi.org/10.1016/J.HELIYON.2017.E00374.
[27] M. Peron, P.C. Skaret, A. Fabrizi, A. Varone, R. Montanari, H.J. Roven, P. Ferro, F. Berto, J. Torgersen, The effect of Equal Channel Angular Pressing on the stress corrosion cracking susceptibility of AZ31 alloy in simulated body fluid, J. Mech. Behav. Biomed. Mater. (2020) 103724, , https://doi.org/10.1016/j.jmbbm.2020.103724.
[28] K.R. Gopi, H.S. Nayaka, S. Sahu, Corrosion behavior of ECAP-processed AM90 magnesium alloy, Arab. J. Sci. Eng. 43 (2018) 4871–4878, https://doi.org/10.1007/s13369-018-3203-5.
[29] B. Ratna Sunil, T.S. Sampath Kumar, U. Chakkingal, V. Nandakumar, M. Doble, V. Devi Prasad, M. Raghunath, In vitro and in vivo studies of biodegradable fine grained AZ31 magnesium alloy produced by equal channel angular pressing, Mater. Sci. Eng. C. 59 (2016) 356–367, https://doi.org/10.1016/J.MSEC.2015.10.028.
[30] S. Dobatkin, N. Martynenko, N. Anisimova, M. Kiselevskiy, D. Prosvirnin, V. Terentiev, N. Yurchenko, G. Salishchev, Y. Estrin, Mechanical properties, biodegradation, and biocompatibility of ultrafine grained magnesium alloy WE43, Materials (Basel) 12 (2019), https://doi.org/10.3390/ma12213627.
[31] M. Peron, R. Bertolini, A. Ghiotti, J. Torgersen, S. Bruschi, F. Berto, Enhancement of stress corrosion cracking of AZ31 magnesium alloy in simulated body fluid thanks to cryogenic machining, J. Mech. Behav. Biomed. Mater. 101 (2020) 103429, , https://doi.org/10.1016/J.JMBBM.2019.103429.
[32] R. Smeets, B. Stadlinger, F. Schwarz, B. Beck-Broichsitter, O. Jung, C. Precht, F. Kloss, A. Gröbe, M. Heiland, T. Ebker, T. Ebker, Impact of dental implant surface modifications on osseointegration, Biomed. Res. Int. 2016 (2016) 1–16, https://doi.org/10.1155/2016/6285620.
[33] T. Albrektsson, A. Wennerberg, Oral implant surfaces: part 1–review focusing on topographic and chemical properties of different surfaces and in vivo responses to them., Int. J. Prosthodont. 17 (n.d.) 536–43. http://www.ncbi.nlm.nih.gov/pubmed/15543910 (accessed October 30, 2017).
[34] J. M.Rúa, A.A. Zuleta, J. Ramírez, P. Fernández-Morales, Micro-arc oxidation coating on porous magnesium foam and its potential biomedical applications, Surf. Coatings Technol. 360 (2019) 213–221, https://doi.org/10.1016/j.surfcoat.2018.12.106.
[35] C. Gao, S. Peng, P. Feng, C. Shuai, Bone biomaterials and interactions with stem cells, Bone Res 5 (2017) 1–33, https://doi.org/10.1038/boneres.2017.59.
[36] T.S.N. Sankara Narayanan, I.-S. Park, M.H. Lee, Surface modification of magnesium and its alloys for biomedical applications, Modification and Coating Techniques, Volume 2 2015.
[37] I.S. Abela, Physical vapour deposition on mg alloys for biomedical applications, Surf. Modif. Magnes. Its Alloy. Biomed. Appl, Elsevier Inc, 2015, pp. 81–100, , https://doi.org/10.1016/B978-1-78242-078-1.00004-9.
[38] W. Jin, G. Wang, X. Peng, W. Li, A.M. Qasim, P.K. Chu, Tantalum nitride films for corrosion protection of biomedical Mg-Y-RE alloy, J. Alloys Compd. 764 (2018) 947–958, https://doi.org/10.1016/J.JALLCOM.2018.06.151.
[39] W. Jin, G. Wang, A.M. Qasim, S. Mo, Q. Ruan, H. Zhou, W. Li, P.K. Chu, Corrosion protection and enhanced biocompatibility of biomedical Mg-Y-RE alloy coated with tin dioxide, Surf. Coatings Technol. 357 (2019) 78–82, https://doi.org/10.1016/j.surfcoat.2018.10.005.
[40] X. Liu, Q. Yang, Z. Li, W. Yuan, Y. Zheng, Z. Cui, X. Yang, K.W.K. Yeung, S. Wu, A combined coating strategy based on atomic layer deposition for enhancement of corrosion resistance of AZ31 magnesium alloy, Appl. Surf. Sci. 434 (2018) 1101–1111, https://doi.org/10.1016/J.APSUSC.2017.11.032.
[41] E. Marin, A. Lanzutti, L. Guzman, L. Fedrizzi, Chemical and electrochemical characterization of TiO2/Al2O3 atomic layer depositions on AZ-31 magnesium alloy, J. Coatings Technol. Res. 9 (2012) 347–355, https://doi.org/10.1007/s11998-011-9372-8.
[42] Q. Yang, W. Yuan, X. Liu, Y. Zheng, Z. Cui, X. Yang, H. Pan, S. Wu, Atomic layer deposited ZrO2 nanofilm on Mg-Sr alloy for enhanced corrosion resistance and biocompatibility, Acta Biomater. 58 (2017) 515–526, https://doi.org/10.1016/J.ACTBIO.2017.06.015.
[43] T. Kasuga, H. Kondo, M. Nogami, Apatite formation on TiO2 in simulated body fluid, J. Cryst. Growth 235 (2002) 235–240, https://doi.org/10.1016/S0022-0248(01)01782-1.
[44] X.X. Wang, S. Hayakawa, K. Tsuru, A. Osaka, Bioactive titania gel layers formed by chemical treatment of Ti substrate with a H2O2/HCl solution, Biomaterials 23 (2002) 1353–1357, https://doi.org/10.1016/S0142-9612(01)00254-X.
[45] M. Uchida, H.-M. Kim, T. Kokubo, T. Nakamura, Apatite-forming ability of titania gels with different structures, Bioceramics, WORLD SCIENTIFIC, 1999, pp. 149–152, , https://doi.org/10.1142/9789814291064_0036.
[46] J.-M. Wu, S. Hayakawa, K. Tsuru, A. Osaka, Low-temperature preparation of anatase and rutile layers on titanium substrates and their ability to induce in vitro apatite deposition, J. Am. Ceram. Soc. 87 (2004) 1635–1642, https://doi.org/10.1111/j.1551-2916.2004.01635.x.
[47] ASTM G5 - 14 Standard Reference Test Method for Making Potentiodynamic Anodic Polarization Measurements, (n.d.). https://compass.astm.org/Standards/HISTORICAL/G5-14.htm (accessed December 3, 2019).
[48] T. Kokubo, H. Takadama, How useful is SBF in predicting in vivo bone bioactivity? Biomaterials 27 (2006) 2907–2915, https://doi.org/10.1016/J.BIOMATERIALS.2006.01.017.
[49] G. Song, A. Atrens, D. StJohn, An hydrogen evolution method for the estimation of the corrosion rate of magnesium alloys, Magnes. Technol, John Wiley & Sons, Inc, Hoboken, NJ, USA, 2001, pp. 254–262, , https://doi.org/10.1002/9781118805497.ch44 2013.
[50] Y. Shi, M. Qi, Y. Chen, P. Shi, MAO-DCPD composite coating on Mg alloy for degradable implant applications, Mater. Lett. 65 (2011) 2201–2204, https://doi.org/10.1016/J.MATLET.2011.04.037.
[51] S. Johnston, Z. Shi, A. Atrens, The influence of pH on the corrosion rate of high-purity Mg, AZ91 and ZE41 in bicarbonate buffered Hanks' solution, Corros. Sci. 101 (2015) 182–192, https://doi.org/10.1016/J.CORSCI.2015.09.018.
[52] S. Nezar, N. Saoula, S. Sali, M. Faiz, M. Mekki, N.A. Laoufi, N. Tabet, Properties of TiO 2 thin films deposited by rf reactive magnetron sputtering on biased substrates, Appl. Surf. Sci. 395 (2017) 172–179, https://doi.org/10.1016/j.apsusc.2016.08.125.
[53] J.H. Kim, S. Lee, H.S. Im, Effect of target density and its morphology on TiO2 thin films grown on Si(100) by PLD, Appl. Surf. Sci. 151 (1999) 6–16, https://doi.org/10.1016/S0169-4332(99)00269-X.
[54] J. Yu, X. Zhao, J. Du, W. Chen, Preparation, microstructure and photocatalytic activity of the porous TiO2 anatase coating by sol-gel processing, J. Sol-Gel Sci. Technol. 17 (2000) 163–171, https://doi.org/10.1023/A:1008703719929.
[55] Y. Xin, K. Huo, T. Hu, G. Tang, P.K. Chu, Corrosion products on biomedical magnesium alloy soaked in simulated body fluids, J. Mater. Res. 24 (2009) 2711–2719, https://doi.org/10.1557/jmr.2009.0323.
[56] Q. Zhang, Y. Jiang, Y. Zhang, Z. Ye, W. Tan, M. Lang, Effect of porosity on long-term degradation of poly (ε-caprolactone) scaffolds and their cellular response, Polym. Degrad. Stab. 98 (2013) 209–218, https://doi.org/10.1016/j.polymdegradstab.2012.10.008.
[57] C. Hadjicharalambous, O. Prymak, K. Loza, A. Buyakov, S. Kulkov, M. Chatzinikolaidou, Effect of porosity of alumina and zirconia ceramics toward pre-osteoblast response, Front. Bioeng. Biotechnol. 3 (2015) 175, https://doi.org/10.3389/fbioe.2015.00175.
[58] J. Munemasa, T. Kumakiri, Effect of the surface roughness of substrates on the corrosion properties of films coated by physical vapour deposition, Surf. Coatings Technol. 49 (1991) 496–499, https://doi.org/10.1016/0257-8972(91)90106-7.
[59] V. Karageorgiou, D. Kaplan, Porosity of 3D biomaterial scaffolds and osteogenesis, Biomaterials 26 (2005) 5474–5491, https://doi.org/10.1016/j.biomaterials.2005.02.002.
[60] F.J. O'Brien, B.A. Harley, M.A. Waller, I.V. Yannas, L.J. Gibson, P.J. Prendergast, The effect of pore size on permeability and cell attachment in collagen scaffolds for tissue engineering, Technol. Heal. Care, IOS Press, 2007, pp. 3–17, , https://doi.

org/10.3233/thc-2007-15102.
[61] A. Pardo, S. Feliu, M.C. Merino, R. Arrabal, E. Matykina, Electrochemical estimation of the corrosion rate of magnesium/aluminium alloys, Int. J. Corros. 2010 (2010), https://doi.org/10.1155/2010/953850.
[62] M. Lorenzetti, E. Pellicer, J. Sort, M.D. Baró, J. Kovač, S. Novak, S. Kobe, Improvement to the corrosion resistance of Ti-based implants using hydrothermally synthesized nanostructured anatase coatings, Materials (Basel) 7 (2014) 180–194, https://doi.org/10.3390/ma7010180.
[63] S. Il Pyun, Y.G. Yoon, E. Lugscheider, R. Mathesius, Relationship between interfacial reaction and adhesion at PVD TiO2 film-metal (Ti or Al) interfaces, Surf. Coatings Technol. 61 (1993) 233–237, https://doi.org/10.1016/0257-8972(93)90231-C.
[64] C. (Christoph) Leyens, M. (Manfred) Peters, John Wiley & Sons, Wiley InterScience (Online Service), Titanium and Titanium Alloys: Fundamentals and Applications, Wiley-VCH, 2003.
[65] H. Hayashi, T. Saitou, N. Maruyama, H. Inaba, K. Kawamura, M. Mori, Thermal expansion coefficient of yttria stabilized zirconia for various yttria contents, Solid State Ionics 176 (2005) 613–619, https://doi.org/10.1016/j.ssi.2004.08.021.
[66] D.R. Hummer, P.J. Heaney, J.E. Post, Thermal expansion of anatase and rutile between 300 and 575 K using synchrotron powder X-ray diffraction, Powder Diffract. 22 (2007) 352–357, https://doi.org/10.1154/1.2790965.
[67] Y. Xu, Y. Zhang, T. He, K. Ding, X. Huang, H. Li, J. Shi, Y. Guo, J. Zhang, The effects of thermal and atmospheric pressure radio frequency plasma annealing in the crystallization of TiO2 thin films, Coatings 9 (2019) 357, https://doi.org/10.3390/coatings9060357.
[68] N. Kumar, T.M. Wilkinson, C.E. Packard, M. Kumar, Design of low surface roughness-low residual stress-high optoelectronic merit a-IZO thin films for flexible OLEDs Articles you may be interested in, J. Appl. Phys. 119 (2016) 225303, , https://doi.org/10.1063/1.4953212.
[69] P. Yáñez-Contreras, J.D.O. Barceinas-Sánchez, C.A. Poblano-Salas, J.M. Medina-Flores, A.L. García-García, I. Domínguez-López, Estudio de la evolución del perfil de esfuerzos residuales en recubrimientos barrera térmica depositados sobre acero inoxidable AISI 304, DYNA 83 (2016) 160–166, https://doi.org/10.15446/dyna.v83n197.51150.
[70] H.J. Moon, Development of Thin Film Inorganic Membranes for Oxygen Separation, Forschungszentrum Jülich, 2012.
[71] Robert B. Heimann, H.D. Lehmann, Bioceramic Coatings for Medical Implants: Trends and Techniques, n.d.
[72] ISO - ISO 25178-2:2012 - Geometrical product specifications (GPS) — surface texture: areal — part 2: terms, definitions and surface texture parameters, (n.d.). https://www.iso.org/standard/42785.html (accessed February 7, 2020).